communications physics

ARTICLE

https://doi.org/10.1038/s42005-021-00791-1 OPEN

Observation of the crossover between metallic and insulating regimes of the spin Hall effect

Hiroyuki Moriya[1], Akira Musha[1], Satoshi Haku[1] & Kazuya Ando[1,2,3]✉

The physics of the anomalous and spin Hall effects is one of the most intriguing aspects of condensed matter physics. An important finding from a large collection of experimental and theoretical results is the universal scaling of the anomalous or spin Hall conductivity with the electric conductivity. This scaling has been successfully described by the intrinsic Berry curvature and extrinsic scattering mechanisms for metallic systems, revealing the topological nature of these effects. In contrast, the underlying physics in the opposite limit, the disordered insulating regime, is still unclear. In particular, it remains a major challenge, both experimentally and theoretically, to explore the spin Hall effect in the insulating regime. Here, we report the observation of the crossover between the metallic and insulating regimes of the spin Hall effect. The result demonstrates a direct correspondence between the spin and anomalous Hall effects, which will advance the fundamental understanding of spin transport.

[1] Department of Applied Physics and Physico-Informatics, Keio University, Yokohama 223-8522, Japan. [2] Keio Institute of Pure and Applied Sciences, Keio University, Yokohama 223-8522, Japan. [3] Center for Spintronics Research Network, Keio University, Yokohama 223-8522, Japan. ✉email: ando@appi.keio.ac.jp

The family of Hall effects has played a central role in the development of condensed matter physics[1–6]. An important member of this family is the spin Hall effect (SHE), which was theoretically predicted about half a century ago[7]. The SHE has attracted extensive attention for its fascinating topological, relativistic, and quantum mechanical nature, as well as spintronics applications[3,8]. This effect enables electric generation and detection of spin currents in solid-state devices, providing an avenue for discovering a variety of spintronics phenomena[3].

The SHE in metallic systems arises from intrinsic and extrinsic contributions, the mechanisms that are also responsible for the anomalous Hall effect (AHE) in ferromagnets[2]. The intrinsic contribution can be explained by the Berry curvature associated with the Fermi surface and the band structure of the materials. On the other hand, the extrinsic contribution is caused by spin-dependent scattering on structural defects or impurities. For the AHE, a large collection of experimental results on a wide class of ferromagnets has revealed that there are three different regimes[2], characterized by the power-law relation, $\sigma_{xy} \propto \sigma_{xx}^{\gamma}$, between the anomalous Hall conductivity σ_{xy} and the longitudinal conductivity σ_{xx}; (i) the superclean regime, where $\sigma_{xy} \propto \sigma_{xx}$ due to the dominant contribution from the skew-scattering, (ii) the moderately dirty regime, where the intrinsic mechanism is dominant, and σ_{xy} is roughly insensitive to σ_{xx}, and (iii) the dirty regime with the scaling exponent γ generically larger than unity. The discovery of the crossover of the AHE has provided important information for the fundamental understanding of the physics of spin transport. Recently, the crossover between these regimes has also been confirmed for the SHE[9–11], demonstrating an important correspondence between the AHE and SHE in the metallic regime.

Although the existing theories have been successful in describing the AHE and SHE in metallic systems based on the intrinsic Berry curvature or the extrinsic scattering mechanisms, it remains a major challenge to understand the full-range phase diagram of these phenomena. The last important step is to explore the AHE and SHE in disordered insulating systems, where the carrier transport is dominated by hopping. In the insulating regime, the scaling relation is nontrivial because the mechanism of the AHE and SHE in hopping systems is clearly different from that in metallic systems; in the insulating regime, the AHE is attributed to a phase that a carrier gains when hopping around closed-loop paths in the presence of spin-orbit coupling (SOC) and background magnetization of the localized moments[12,13]. Nevertheless, experimental observations have demonstrated that the scaling of the anomalous Hall conductivity with the electric conductivity prevails not only in the dirty metallic regime but also deep into the disordered insulating hopping regime[2]. An analogous trend is expected for the SHE because of the similarity in the underlying physics. However, in contrast to the large collection of experimental results for the AHE, it remains a major experimental challenge to explore the SHE in the disordered insulating regime.

In this work, we report the observation of the crossover between the metallic and insulating regimes of the SHE in Pt, a model system for the study of the SHE. To explore the SHE in the insulating regime, the electric conductivity of Pt films is varied by three orders of magnitude by incorporating oxygen. We find the scaling behavior of the spin Hall conductivity, which prevails not only in the dirty metallic regime but also in the disordered insulating regime, despite the distinct difference in the transport mechanism. The observed variation of the spin Hall conductivity over the wide range of electric conductivity is reminiscent of the scaling of the anomalous Hall conductivity, illustrating a direct correspondence between the SHE and AHE in both the metallic and insulating regimes.

Results

Transport measurement. We use the spin-torque ferromagnetic resonance (ST-FMR)[14–16] to study the SHE of PtO_x films with various oxidation levels. Figure 1a shows a schematic illustration of the device. The device structure is SiO_2(4 nm)/$Ni_{81}Fe_{19}$(d_F)/TiN(2 nm)/PtO_x(10 nm)/SiO_2-substrate, where the numbers in parentheses represent the thickness (for details, see "Methods"). The separation between the $Ni_{81}Fe_{19}$ and PtO_x layers by the insertion layer minimizes the interfacial SOC effects, including the spin memory loss and interfacial spin-orbit torques[17,18]. To minimize possible oxidation effects on the insertion layer due to its proximity to the PtO_x layer, we chose TiN, which is less susceptible to oxidation[19], instead of other light metals, such as Cu and Ti. We can neglect the spin relaxation in the insertion layer because of the long spin diffusion length of around 40 nm in TiN due to the weak SOC[20]. In the $Ni_{81}Fe_{19}$/TiN/PtO_x device, to control the oxidation level of the PtO_x layer, argon and oxygen gases were introduced into the chamber during the sputtering of the PtO_x film, and the amount of oxygen gas in the reactive mixture, Q, was varied between 0 and 10%. As shown in Fig. 1b, the electric resistivity ρ_N of the PtO_x film increases with Q, indicating that the oxidation level of the PtO_x layer is controlled by tuning Q. The change in the oxidation level induced by tuning Q is supported by X-ray photoelectron spectroscopy (XPS) spectra, shown in Fig. 1c.

To characterize the carrier transport in the PtO_x films with different oxidation levels, we measured temperature T dependence of the sheet resistance R_s for the PtO_x films. Figure 2a shows the T dependence of R_s for the PtO_x film with $Q = 1\%$. This result shows that R_s decreases monotonically with decreasing

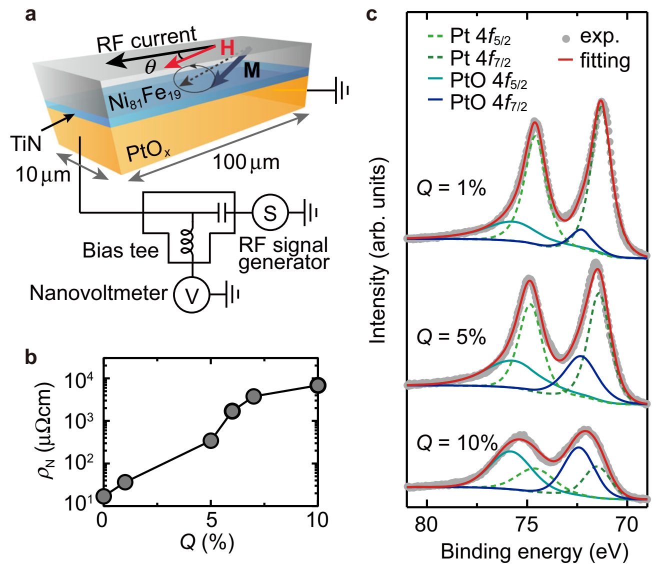

Fig. 1 Device structure. a Schematic illustration of the SiO_2/$Ni_{81}Fe_{19}$/TiN/PtO_x/SiO_2-substrate device used for the spin-torque ferromagnetic resonance (ST-FMR) measurement. θ is the angle between the direction of the radio frequency (RF) current and the in-plane applied magnetic field **H**. **M** denotes the magnetization, and the letters S and V in the illustration denote the RF signal generator and the nanovoltmeter, respectively. **b** Oxygen-gas flow ratio Q dependence of the electric resistivity ρ_N, measured by the standard four-probe method, of the PtO_x film. **c** X-ray photoelectron spectroscopy (XPS) spectra for the PtO_x films with $Q = 1$, 5, and 10%. The gray curve is the experimental data (exp.), and the red curve is the fitting result. The binding energies of the Pt $4f_{7/2}$ peak for Pt, PtO, and PtO_2 are around 71.3, 72.3, 74.0 eV, respectively[48].

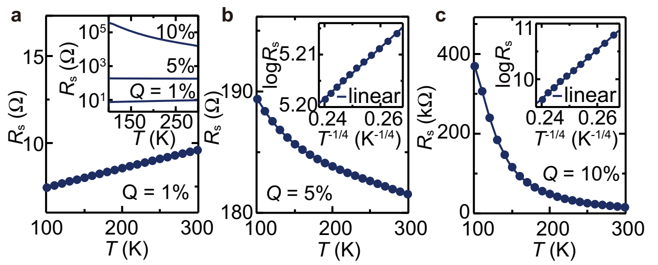

Fig. 2 Transport mechanism. Temperature T dependence of the sheet resistance R_s for the PtO_x films with **a** $Q = 1\%$, **b** $Q = 5\%$, and **c** $Q = 10\%$. We also compare the T dependence of R_s for the films with different Q in the inset to (**a**). The insets in **b**, **c** show $T^{-1/4}$ dependence of $\log R_s$, where $200\,\mathrm{K} \leq T \leq 300\,\mathrm{K}$. The solid circles are the experimental data and the solid lines are the linear fitting results.

T: $dR_s/dT > 0$, showing a typical metallic behavior. By increasing the oxidation level, the T dependence of R_s is clearly changed. As shown in Fig. 2b and c, R_s increases with decreasing T for the PtO_x film with $Q = 5\%$ and $Q = 10\%$: $dR_s/dT < 0$.

To clarify the transport mechanism in the PtO_x films around room temperature, we plot $\log R_s$ as a function of $T^{-1/4}$ (see the inset to Fig. 2b and c). This result shows that, for $200\,\mathrm{K} \leq T \leq 300\,\mathrm{K}$, the T dependence of R_s is well described by the Mott variable range hopping (Mott-VRH) mechanism[21]:

$$R_s = R_{\mathrm{Mott}} \exp\left[\left(\frac{T_{\mathrm{Mott}}}{T}\right)^{1/4}\right], \tag{1}$$

where R_{Mott} and T_{Mott} are the resistance parameter and the Mott characteristic temperature, respectively. This result indicates that the PtO_x film with $Q = 5\%$ is near the crossover between the band and hopping transport regimes, and the transport in the PtO_x film with $Q = 10\%$ is dominated by the Mott-VRH.

Spin-torque ferromagnetic resonance. Figure 3a shows the ST-FMR spectra for the $Ni_{81}Fe_{19}$(8 nm)/TiN(2 nm)/PtO_x(10 nm) trilayers with $Q = 0$, 6, and 10%, measured at room temperature. For the measurement, a radio frequency (RF) charge current was applied along the longitudinal direction of the device, and an in-plane external magnetic field H was applied with an angle of $\theta = 45°$ from the longitudinal direction (see also Fig. 1a). In the trilayer, the RF current generates damping-like (DL) and field-like (FL) spin-orbit torques, as well as an Oersted field, which drive magnetization precession in the $Ni_{81}Fe_{19}$ layer under the FMR condition. The magnetization precession induces an oscillation of the resistance due to the anisotropic magnetoresistance, resulting in the generation of a direct current (DC) voltage V_{DC} through the mixing of the RF charge current and oscillating resistance[14,15]:

$$V_{\mathrm{DC}} = V_{\mathrm{sym}} \frac{W^2}{(\mu_0 H - \mu_0 H_{\mathrm{res}})^2 + W^2} + V_{\mathrm{antisym}} \frac{W(\mu_0 H - \mu_0 H_{\mathrm{res}})}{(\mu_0 H - \mu_0 H_{\mathrm{res}})^2 + W^2}, \tag{2}$$

where W is the linewidth and H_{res} is the FMR field. Here, V_{sym} and V_{antisym} are the magnitude of the symmetric and antisymmetric components, respectively; V_{sym} is proportional to the out-of-plane effective field $H_\perp$, which is dominated by the DL spin-orbit effective field H_{DL}, while V_{antisym} is proportional to the in-plane effective field $H_\parallel$, which is the sum of the Oersted field H_{Oe} and FL spin-orbit effective field H_{FL}. As shown in Fig. 3a, the V_{DC} spectrum varies systematically by changing the RF frequency f. We have confirmed that the variation of the resonance field H_{res} is consistent with the Kittel formula: $(2\pi f/\gamma) = \sqrt{\mu_0 H_{\mathrm{res}}(\mu_0 H_{\mathrm{res}} + \mu_0 M_{\mathrm{eff}})}$, where M_{eff} is the effective demagnetization field and γ is the gyromagnetic ratio.

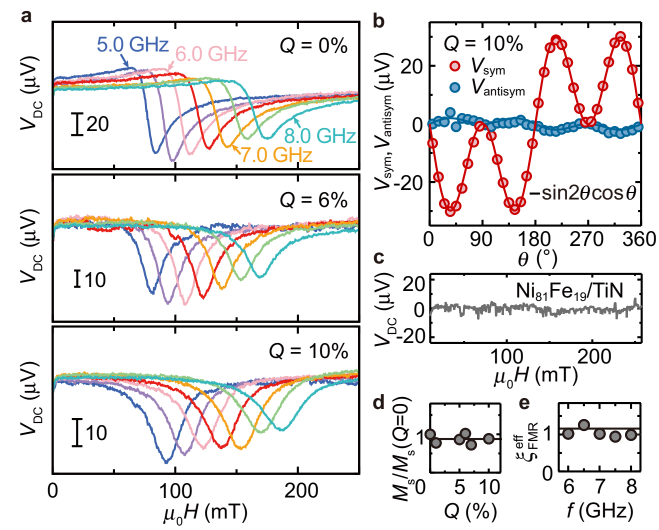

Fig. 3 Spin-torque ferromagnetic resonance. a Magnetic field H dependence of the direct current (DC) voltage V_{DC} for the $Ni_{81}Fe_{19}$/TiN/PtO_x films with $Q = 0$, 6, and 10% at the frequencies from 5.0 to 8.0 GHz with an applied radio frequency (RF) power of 20 dBm. The $Ni_{81}Fe_{19}$-layer thickness is $d_F = 8$ nm. **b** In-plane magnetic field angle θ dependence of the V_{sym} (red) and V_{antisym} (blue) components of the spin-torque ferromagnetic resonance (ST-FMR) signal at $f = 6.5$ GHz for the $Ni_{81}Fe_{19}$/TiN/PtO_x film with $Q = 10\%$. Here, θ is defined as the angle between the direction of the RF current and the in-plane applied magnetic field. The circles are the experimental data. Error bars, which represent the standard deviation of the fitting procedure, are smaller than the symbols. The solid curves are the fitting result using a function proportional to $\sin 2\theta \cos\theta$. **c** H dependence of V_{DC} at $f = 7.5$ GHz with an applied RF power of 20 dBm for the $Ni_{81}Fe_{19}$/TiN film, where the PtO_x layer is absent. **d** Q dependence of $M_s/M_s(Q = 0)$, where $M_s(Q = 0)$ is the saturation magnetization of the $Ni_{81}Fe_{19}$/TiN/PtO_x film with $Q = 0\%$. The black line is a guide to the eye. **e** Frequency f dependence of $\xi^{\mathrm{eff}}_{\mathrm{FMR}}$ for the $Ni_{81}Fe_{19}$/TiN/PtO_x film with $Q = 10\%$ and $d_F = 12$ nm. The black line is a guide to the eye.

The ST-FMR signals observed for the $Ni_{81}Fe_{19}$/TiN/PtO_x films originate from the RF current flowing in the PtO_x layer. In Fig. 3b, we show magnetic field angle θ dependence of the symmetric V_{sym} and antisymmetric V_{antisym} components, extracted by fitting the measured V_{DC} using Eq. (2), where θ is defined as the angle between the direction of the RF current and the in-plane applied magnetic field $\mathbf{H}$ (see Fig. 1a). Figure 3b shows that V_{antisym} is proportional to $\sin 2\theta \cos\theta$. This result indicates that the in-plane effective field, $H_\parallel = H_{\mathrm{FL}} + H_{\mathrm{Oe}}$, is independent of θ, which is consistent with that H_{FL} and H_{Oe} are independent of the magnetization direction (see also Supplementary Note 1)[15,22,23]. We note that V_{sym} is also proportional to $\sin 2\theta \cos\theta$. This result indicates that the out-of-plane effective field, $H_\perp$, is proportional to $\cos\theta$, (see also Supplementary Note 1)[15,22,23]. The angular dependence of $H_\perp$ is consistent with the prediction of the out-of-plane effective field generated by the SHE: $H_\perp = H_{\mathrm{DL}}|\mathbf{m} \times \boldsymbol{\sigma}| = H_{\mathrm{DL}} \cos\theta$, where $\mathbf{m}$ and $\boldsymbol{\sigma}$ are the unit vectors of the magnetization in the $Ni_{81}Fe_{19}$ layer and the spin polarization direction of the spin current generated by the SHE in the PtO_x layer, respectively[22]. We also note that the V_{DC} signal disappears in a $Ni_{81}Fe_{19}$(8 nm)/TiN(2 nm) film, where the PtO_x layer is absent, as shown in Fig. 3c. This result shows that the anomalous spin-orbit torque in the $Ni_{81}Fe_{19}$ layer, as well as the spin-orbit torques generated by the TiN layer is negligible in the

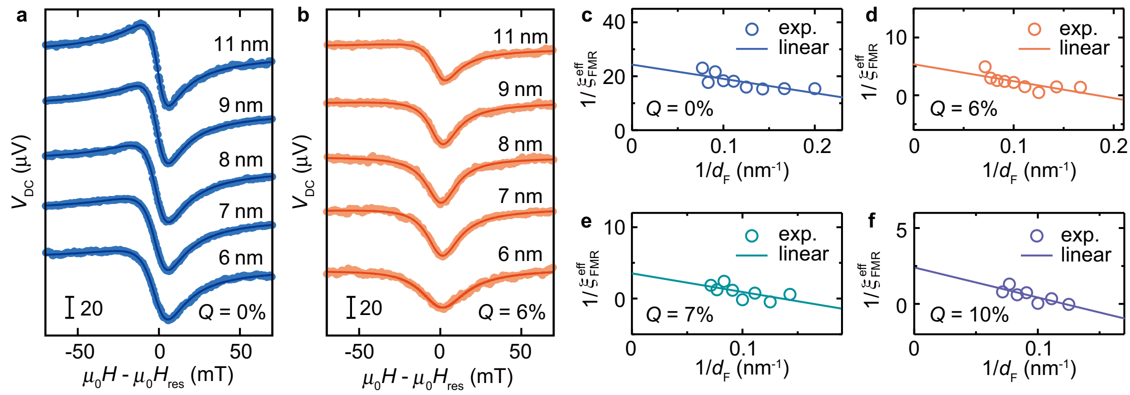

Fig. 4 Spin-torque ferromagnetic resonance for devices with different thickness. Spin-torque ferromagnetic resonance (ST-FMR) spectra for the $Ni_{81}Fe_{19}$/TiN/PtO_x films with **a** $Q = 0\%$ and **b** $Q = 6\%$ at 6.5 GHz, where d_F is the thickness of the $Ni_{81}Fe_{19}$ layer. H_{res} is the FMR field. The solid circles are the experimental data and the solid curves are the fitting results using Eq. (2). $1/d_F$ dependence of $1/\xi^{eff}_{FMR}$ for the devices with **c** $Q = 0\%$, **d** $Q = 6\%$, **e** $Q = 7\%$, and **f** $Q = 10\%$. The open circles are the experimental data (exp.). Error bars, which represent the standard deviation of the fitting procedure, are smaller than the symbols. The solid lines are the linear fitting results.

$Ni_{81}Fe_{19}$/TiN/PtO_x films. The interfacial spin-orbit torques originating at the TiN/PtO_x interface also play a minor role in the $Ni_{81}Fe_{19}$/TiN/PtO_x film because interfacial SOC effects are notable only when PtO_x is directly contacted with $Ni_{81}Fe_{19}$[18]. These results indicate that the sizable symmetric voltage V_{DC} observed for the $Ni_{81}Fe_{19}$/TiN/PtO_x films originates from the DL torque generated by the SHE in the PtO_x layer (see also Supplementary Note 2).

The ST-FMR for the $Ni_{81}Fe_{19}$/TiN/PtO_x films allows us to quantify the DL-torque efficiency due to the SHE in the PtO_x layer. For the trilayer, we define the effective FMR spin-torque efficiency as ref. [24]

$$\xi^{eff}_{FMR} = \frac{V_{sym}}{V_{antisym}} \frac{e\mu_0 M_s d_F d_N^{eff}}{\hbar} \sqrt{1 + \frac{\mu_0 M_{eff}}{\mu_0 H_{res}}}, \quad (3)$$

where $d_N^{eff} = d_N + (\rho_N/\rho_I)d_I$ is the effective thickness of the nonmagnetic layer. In Eq. (3), $d_N = 10$ nm is the thickness of the PtO_x layer; $d_I = 2$ nm and $\rho_I = 462$ μΩcm are the thickness and resistivity of the TiN layer, respectively. Here, M_s is the saturation magnetization, which is independent of Q as shown in Fig. 3d. The negligible change in M_s with Q shows that the $Ni_{81}Fe_{19}$ layer is not affected by the change of the oxidation level of the PtO_x layer, supporting that the $Ni_{81}Fe_{19}$ and PtO_x layers are well separated by the TiN insertion layer. We have also confirmed that ξ^{eff}_{FMR}, extracted by fitting the V_{DC} spectra, is independent of the frequency f of the applied RF current, as shown in Fig. 3e. The negligible change in ξ^{eff}_{FMR} with f shows that the observed voltage is dominated by the ST-FMR, and possible spin pumping and thermoelectric contributions are negligible in the ST-FMR spectra (see also Supplementary Note 1)[25]. From the effective FMR spin-torque efficiency ξ^{eff}_{FMR}, the DL(FL) torque efficiencies per unit applied electric field E, $\xi^E_{DL(FL)} = (2e/\hbar)\mu_0 M_s d_F H_{DL(FL)}/E$, can be determined using refs. [24,26]

$$\frac{1}{\xi^{eff}_{FMR}} = \frac{1}{\xi^E_{DL}}\left(\frac{1}{\rho_N} + \frac{\hbar}{e}\frac{\xi^E_{FL}}{\mu_0 M_s d_F d_N^{eff}}\right). \quad (4)$$

To determine ξ^E_{DL} using Eq. (4), we measured the ST-FMR for the $Ni_{81}Fe_{19}$/TiN/PtO_x films with different $Ni_{81}Fe_{19}$ layer thicknesses d_F, as shown in Fig. 4a and b. By fitting the measured spectra using Eq. (2), we obtain $1/d_F$ dependence of $1/\xi^{eff}_{FMR}$ for the $Ni_{81}Fe_{19}$/TiN/PtO_x films with different oxidation levels, as shown in Fig. 4c–f. Figure 4c–f show that $1/\xi^{eff}_{FMR}$ changes linearly with $1/d_F$, enabling us to determine the DL torque efficiency ξ^E_{DL} using Eq. (4). Here, the DL-torque efficiency ξ^E_{DL} can be determined from the ST-FMR signals regardless of the transport mechanism in the PtO_x layer. The reason for this is that ξ^E_{DL} is obtained from the measurement of the effective fields acting on the magnetization of the $Ni_{81}Fe_{19}$ layer, and the detection of ST-FMR signals relies on the magnetoresistance of the $Ni_{81}Fe_{19}$ layer; the ST-FMR model does not assume a specific transport mechanism in the non-magnetic layer.

Discussion

Using the ST-FMR result, we investigate the variation of the spin Hall conductivity σ_{SH} in the PtO_x films, where the longitudinal electric conductivity σ_N is varied by three orders of magnitude. Since the SHE in the PtO_x layer dominates the observed DL torque, the effective spin Hall conductivity σ^*_{SH} of the PtO_x layer can be determined directly from the extracted values of ξ^E_{DL} using

$$\sigma^*_{SH} = \left(\frac{\hbar}{2e}\right)\xi^E_{DL}. \quad (5)$$

The effective spin Hall conductivity σ^*_{SH} is related to the spin Hall conductivity σ_{SH} as $\sigma_{SH} = (1/T_{int})\sigma^*_{SH}$, where T_{int} is the spin transparency. We show the variation of σ^*_{SH} in Fig. 5 (see the open circles in red). This result shows that σ^*_{SH} is clearly suppressed by increasing the oxidation level when $Q \geq 5\%$, while σ^*_{SH} is almost unchanged by changing Q from 0–1%. The significant change in σ^*_{SH} when $Q \geq 5\%$ indicates that the spin Hall conductivity σ_{SH} is suppressed with increasing the oxidation level of the PtO_x layer.

For the metallic PtO_x ($Q = 0$ and 1%), the spin transparency T_{int} in the $Ni_{81}Fe_{19}$/TiN/PtO_x film is described by the framework based on the spin diffusion model (see also Supplementary Note 3):

$$T_{int} = \frac{1 - \mathrm{sech}(\delta_N)}{G_I \sinh(\delta_I) + G_N \cosh(\delta_I)\tanh(\delta_N)} \frac{G_F \tanh\delta_F}{1 + (G_F/G'_{ext})\tanh\delta_F}, \quad (6)$$

where $\delta_i = d_i/\lambda_i$, $G_i = \sigma_i/\lambda_i$, and $G'_{ext} = G_I\left[\frac{G_I \coth(\delta_N) + G_N \coth(\delta_I)}{G_I \coth(\delta_N)\coth(\delta_I) + G_N}\right]$. Here, λ_i is the spin diffusion length and σ_i is the longitudinal electric conductivity of the i(=F, I, and N) layer, where F, I, and N correspond to $Ni_{81}Fe_{19}$, TiN, and PtO_x, respectively. Using[27,28] $G_F = 1.1 \times 10^{15}\ \Omega^{-1}\ m^{-2}$ and $G_N = 1.6 \times 10^{15}\ \Omega^{-1}\ m^{-2}$ with measured values of σ_i, we obtain $T_{int} = 0.35$ for $Q = 0\%$. By increasing Q, the transparency T_{int} increases due to suppression of the spin

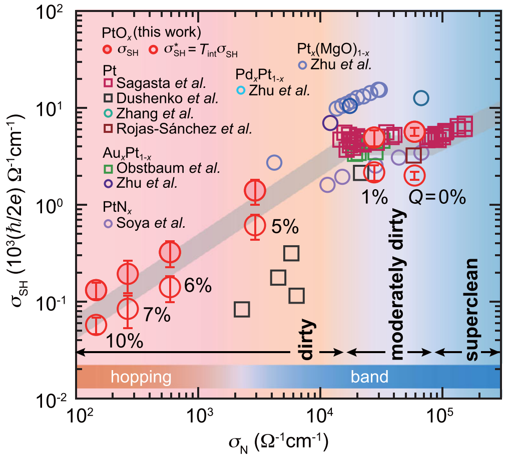

Fig. 5 Scaling of spin Hall conductivity. The spin Hall conductivity $\sigma_{\rm SH}$ of Pt and Pt-based alloys plotted as a function of the longitudinal electric conductivity $\sigma_{\rm N}$. The solid circles in red are the experimental result of this work. The effective spin Hall conductivity $\sigma^*_{\rm SH} = \left(\frac{\hbar}{2e}\right)\xi^E_{\rm DL}$ is also plotted (open circles in red). The error bars are the standard deviation. Other data are taken from published papers: Pt[9,10,25,49], PtN_x[50], Pd_xPt_{1-x}[39], $Pt_x(MgO)_{1-x}$[11], and Au_xPt_{1-x}[40,51]. The open circles and open squares represent the data obtained from spin Hall effect (SHE) and inverse SHE measurements, respectively. For results where $\sigma_{\rm SH}$ is not explicitly shown, we estimated $\sigma_{\rm SH}$ from the spin Hall angle. The gray line is a guide for the eyes. The different background colors represent different regimes of the SHE: the superclean regime (blue), moderately dirty metallic regime (light blue), dirty metallic regime (orange), and disordered insulating regime (pink).

conductance $G_{\rm N}$ because $G_{\rm N}$ is proportional to the carrier density and independent of the carrier scattering time[11]. By taking into account the change of the carrier density, determined from Hall measurements, and assuming a dominant Elliott-Yafet spin relaxation mechanism, we obtain $T_{\rm int} = 0.44$ for $Q = 1\%$. In Fig. 5, we plot the spin Hall conductivity, determined from $\sigma_{\rm SH} = (1/T_{\rm int})\sigma^*_{\rm SH}$ (see the solid circles in red). Figure 5 shows that $\sigma_{\rm SH}$ is almost independent of $\sigma_{\rm N}$ when $\sigma_{\rm N}$ is in the range of around $2\times10^4\,\Omega^{-1}\,{\rm cm}^{-1}$ to $8\times10^4\,\Omega^{-1}\,{\rm cm}^{-1}$. This result is consistent with the prediction of the SHE in the moderately dirty regime, where the dominant mechanism of the SHE is the intrinsic mechanism and the spin Hall conductivity is insensitive to the electric conductivity[2].

The situation is clearly changed by further decreasing the electric conductivity of the PtO_x layer. For the heavily oxidized PtO_x devices, a full description of the spin transparency requires a theoretical framework describing hopping spin transport. However, developing such a framework has been a major challenge for theoretical study and is beyond the scope of the present work. In this work, for simplicity, we adopt the spin-diffusion model for the insulating regime, as well as for the metallic regime. This assumption is supported for organic semiconductors where the transport is dominated by carrier hopping; recent experimental and theoretical studies show that the spin-diffusion model describes well the hopping-dominated spin transport[29–31]. However, for the insulating PtO_x, the validity of describing the hopping spin transport by the spin-diffusion model is unclear. Thus, we estimate $T_{\rm int}$ of the insulating PtO_x systems by extrapolating $T_{\rm int}$ of the metallic PtO_x systems, instead of calculating $T_{\rm int}$ based on the spin-diffusion model using parameters for the PtO_x devices in the hopping regime. Under this assumption, $T_{\rm int} = 0.44$, for $Q = 1\%$, is the lower bound of the transparency for $Q \geq 5\%$ because the decrease of the carrier density decreases $G_{\rm N}$, which increases $T_{\rm int}$ (see Eq. (6)). In Fig. 5, we plot the spin Hall conductivity $\sigma_{\rm SH}$ obtained under the assumption of $T_{\rm int} = 0.44$ for $Q \geq 5\%$. This result demonstrates that $\sigma_{\rm SH}$ decreases rapidly with decreasing $\sigma_{\rm N}$ for $Q \geq 5\%$, showing $\sigma_{\rm SH} \propto \sigma_N^\gamma$ with $\gamma = 0.8$. Since $T_{\rm int}$ is expected to increase with decreasing Q under the above assumption, $\gamma = 0.8$ is the lower bound; γ can be larger than unity if $T_{\rm int}(Q=10\%)/T_{\rm int}(Q=5\%) > 1.9$.

Notable is that the scaling behavior of the spin Hall conductivity prevails not only in the dirty metallic regime but also in the disordered insulating regime. Figure 5 shows that the observed variation of the spin Hall conductivity of the PtO_x film in the insulating hopping regime ($\sigma_{\rm N} < 10^3\,\Omega^{-1}\,{\rm cm}^{-1}$) is similar to that for Pt and Pt-based alloys in the dirty metallic regime (see the data obtained by the present and previous studies in the range of around $2\times10^3\,\Omega^{-1}\,{\rm cm}^{-1}$ to $2\times10^4\,\Omega^{-1}\,{\rm cm}^{-1}$ in Fig. 5). This result is reminiscent of the variation of the anomalous Hall conductivity in the dirty metallic and disordered insulating regimes. In the dirty metallic regime, the anomalous Hall conductivity is suppressed by the disorder due to the influence of finite-lifetime disorder broadening on the intrinsic contribution[32], which explains the scaling of the anomalous Hall conductivity in this regime. This mechanism is also responsible for the scaling of the spin Hall conductivity in the dirty metallic regime[11]. For the AHE, experimental studies have uncovered that the same scaling holds even in the disordered insulating regime, despite the distinct difference in the transport mechanism[2]. In the insulating hopping regime, the AHE arises from interference between direct ($i \to j$) and indirect ($i \to k \to j$) hoppings in a triad, where i and j are pairs of hopping sites, and k is the intermediate hopping site[13]. A similar mechanism can also give rise to the SHE in the insulating regime; the SHE in this regime arises when the hopping via an intermediate site is considered in addition to the hopping between pairs of sites[33]. The observed scaling of the spin Hall conductivity over the wide range of electric conductivity demonstrates an important correspondence between the SHE and the AHE in both the metallic and insulating regimes.

Here, we note that, even for the AHE, the microscopic mechanism in the insulating regime is still not fully understood despite the long history of the experimental and theoretical studies[2]. In contrast to the insulating regime, there is a consensus that the AHE and SHE in the metallic regime can be understood by the intrinsic and extrinsic mechanisms. In establishing the understanding of the AHE and SHE in the metallic regime, extensive experimental studies on the scaling behavior of the anomalous Hall and spin Hall conductivities have played a crucial role. Since the exploration of spin transport in insulating systems has been challenging both experimentally and theoretically, we believe that our experimental demonstration of the scaling of the SHE will stimulate theoretical and computational studies on the spin transport in the insulating hopping regime.

In summary, we have demonstrated the crossover between the metallic and insulating regimes of the SHE by tuning the oxidation level of PtO_x. We found that the spin Hall conductivity in the lightly oxidized PtO_x is almost independent of the electric conductivity, which is consistent with the prediction of the intrinsic SHE in the moderately dirty metallic regime. By further increasing the oxidation level, the PtO_x film enters the dirty regime, where the spin Hall conductivity decreases with decreasing the electric conductivity. We found that the spin Hall conductivity varies systematically despite the drastic change of the transport mechanism; the scaling of the spin Hall conductivity with the electric conductivity prevails not only in the dirty metallic regime but also in the insulating hopping regime. This result is reminiscent of the scaling of the anomalous Hall conductivity. Here, we note that although the SHE and AHE share the similar mechanisms, the relation between the two phenomena is non-trivial. The relation between the SHE and AHE has recently been investigated for ferromagnetic metals[34]. In ferromagnets, both spin and charge accumulations can exist and are detected as the SHE and AHE, respectively[35,36]. Since a charge flow in ferromagnets is spin polarized, an anomalous Hall current is accompanied by a spin current. Thus, it would be natural to expect that the spin polarization relates the AHE and SHE in ferromagnets. In fact, the anomalous Hall conductivity and the spin Hall conductivity, defined by spin-dependent Hall conductivities, are related by the spin polarization in the two-current model, where the Hall current consists of two independent channels formed by the majority and minority spins[36,37]. This simple relation, derived from the model often used to describe the spin transport in ferromagnets, might hold in the limit of diffusive transport with an isotropic spin polarization[36]. However, this simple relation is not valid in general[36,37]. A recent experiment has shown that the relation between the SHE and AHE is complex in ferromagnetic metals[36]. This complication can be attributed to the difference in the spin characters of the bands responsible for the SHE and AHE[38]. Since the SHE and AHE behave differently even in the same system[36], it is not obvious whether there should be a direct correspondence between the scaling relation of the AHE in ferromagnets and that of the SHE in non-magnets in general. Thus, we believe that the observed crossover of the SHE provides essential information for a deeper fundamental understanding of spin-orbit physics and stimulates in-depth theoretical studies of the physics of spin transport in disordered systems. We also note that one of the main challenges of spintronics is exploring approaches to improve the spin-orbit torque efficiency because current-induced spin-orbit torques play a crucial role in a variety of spintronics applications, such as nonvolatile magnetic memories, reconfigurable logics, and neuromorphic computing devices[8,17,24,39–47]. The observed scaling of the spin Hall conductivity provides important information for the development of efficient spin-orbit torque generators.

Methods

Device fabrication. The $Ni_{81}Fe_{19}$/TiN/PtO_x films were deposited on SiO_2 substrates by radio frequency (RF) magnetron sputtering. We first deposited the PtO_x layer on the SiO_2 substrate in a mixed argon and oxygen atmosphere. The amount of the oxygen gas in the reactive mixture Q was varied between 0 and 10%. After the PtO_x deposition, the chamber was evacuated to 2×10^{-5} Pa. Then, the TiN layer was fabricated by introducing 10% nitrogen into the argon gas flow. On the top of the TiN layer, the $Ni_{81}Fe_{19}$ film and a SiO_2 capping layer were sputtered in a pure argon atmosphere. The resistivity of the TiN layer was determined from measured resistance of $Ni_{81}Fe_{19}$(10 nm)/TiN(2 nm) and $Ni_{81}Fe_{19}$(10 nm) films by assuming a two layer parallel circuit model. For the ST-FMR measurement, the $Ni_{81}Fe_{19}$/TiN/PtO_x films were patterned into rectangular strips with a width of 10 μm and length of 100 μm using the photolithography and lift-off techniques.

Data availability

The data that support the findings of this study are available from the corresponding author upon reasonable request.

Received: 30 June 2021; Accepted: 16 December 2021;
Published online: 11 January 2022

References

1. Prange, R. & Girvin, S. M. (eds.) *The Quantum Hall Effect* (Springer, New York, 1990).
2. Nagaosa, N., Sinova, J., Onoda, S., MacDonald, A. H. & Ong, N. P. Anomalous Hall effect. *Rev. Mod. Phys.* **82**, 1539–1592 (2010).
3. Sinova, J., Valenzuela, S. O., Wunderlich, J., Back, C. H. & Jungwirth, T. Spin Hall effects. *Rev. Mod. Phys.* **87**, 1213–1260 (2015).
4. Liu, C.-X., Zhang, S.-C. & Qi, X.-L. The quantum anomalous Hall effect: theory and experiment. *Annu. Rev. Condens. Matter Phys.* **7**, 301–321 (2016).
5. Qi, X.-L. & Zhang, S.-C. Topological insulators and superconductors. *Rev. Mod. Phys.* **83**, 1057–1110 (2011).
6. Nagaosa, N. & Tokura, Y. Topological properties and dynamics of magnetic skyrmions. *Nat. Nanotechnol.* **8**, 899–911 (2013).
7. D'yakonov, M. & Perel, V. Possibility of orienting electron spins with current. *JETP Lett. 13* **13**, 467 (1971).
8. Manchon, A. et al. Current-induced spin-orbit torques in ferromagnetic and antiferromagnetic systems. *Rev. Mod. Phys.* **91**, 035004 (2019).
9. Sagasta, E. et al. Tuning the spin Hall effect of Pt from the moderately dirty to the superclean regime. *Phys. Rev. B* **94**, 060412 (2016).
10. Dushenko, S. et al. Tunable inverse spin Hall effect in nanometer-thick platinum films by ionic gating. *Nat. Commun.* **9**, 3118 (2018).
11. Zhu, L., Zhu, L., Sui, M., Ralph, D. C. & Buhrman, R. A. Variation of the giant intrinsic spin Hall conductivity of Pt with carrier lifetime. *Sci. Adv.* **5**, eaav8025 (2019).
12. Burkov, A. A. & Balents, L. Anomalous Hall effect in ferromagnetic semiconductors in the hopping transport regime. *Phys. Rev. Lett.* **91**, 057202 (2003).
13. Liu, X.-J., Liu, X. & Sinova, J. Scaling of the anomalous Hall effect in the insulating regime. *Phys. Rev. B* **84**, 165304 (2011).
14. Liu, L., Moriyama, T., Ralph, D. C. & Buhrman, R. A. Spin-torque ferromagnetic resonance induced by the spin Hall effect. *Phys. Rev. Lett.* **106**, 036601 (2011).
15. Fang, D. et al. Spin-orbit-driven ferromagnetic resonance. *Nat. Nanotechnol.* **6**, 413–417 (2011).
16. Liu, L. et al. Spin-torque switching with the giant spin Hall effect of tantalum. *Science* **336**, 555–558 (2012).
17. An, H., Kanno, Y., Asami, A. & Ando, K. Giant spin-torque generation by heavily oxidized Pt. *Phys. Rev. B* **98**, 014401 (2018).
18. Asami, A. et al. Spin absorption at a ferromagnetic-metal/platinum-oxide interface. *Phys. Rev. B* **99**, 024432 (2019).
19. Chen, H.-Y. & Lu, F.-H. Oxidation behavior of titanium nitride films. *J. Vac. Sci. Technol. A* **23**, 1006–1009 (2005).
20. An, H. et al. Spin current transport in ceramic: TiN thin film. *Appl. Phys. Lett.* **108**, 121602 (2016).
21. Mott, N. Conduction in glasses containing transition metal ions. *J. Non-Cryst. Solids* **1**, 1–17 (1968).
22. Karimeddiny, S., Mittelstaedt, J. A., Buhrman, R. A. & Ralph, D. C. Transverse and longitudinal spin-torque ferromagnetic resonance for improved measurement of spin-orbit torque. *Phys. Rev. Appl.* **14**, 024024 (2020).
23. Wei, J. et al. Characterization of spin-orbit torque efficiency in magnetic heterostructures with perpendicular magnetic anisotropy via spin-torque ferromagnetic resonance. *Phys. Rev. Appl.* **13**, 034041 (2020).
24. Kageyama, Y. et al. Spin-orbit torque manipulated by fine-tuning of oxygen-induced orbital hybridization. *Sci. Adv.* **5**, eaax4278 (2019).
25. Zhang, W., Han, W., Jiang, X., Yang, S.-H. & S. P. Parkin, S. Role of transparency of platinum–ferromagnet interfaces in determining the intrinsic magnitude of the spin Hall effect. *Nat. Phys.* **11**, 496–502 (2015).
26. Pai, C.-F., Ou, Y., Vilela-Leão, L. H., Ralph, D. C. & Buhrman, R. A. Dependence of the efficiency of spin Hall torque on the transparency of Pt/ferromagnetic layer interfaces. *Phys. Rev. B* **92**, 064426 (2015).
27. Sagasta, E. et al. Spin diffusion length of permalloy using spin absorption in lateral spin valves. *Appl. Phys. Lett.* **111**, 082407 (2017).
28. Nguyen, M.-H., Ralph, D. C. & Buhrman, R. A. Spin torque study of the spin Hall conductivity and spin diffusion length in platinum thin films with varying resistivity. *Phys. Rev. Lett.* **116**, 126601 (2016).
29. Watanabe, S. et al. Polaron spin current transport in organic semiconductors. *Nat. Phys.* **10**, 308–313 (2014).
30. Kimata, M., Nozaki, D., Niimi, Y., Tajima, H. & Otani, Y. Spin relaxation mechanism in a highly doped organic polymer film. *Phys. Rev. B* **91**, 224422 (2015).
31. Lu, Q., Xie, S. & Qu, F. Hopping-dominated spin transport in unintentionally doped organic semiconductors. *J. Phys. Chem. Lett.* **12**, 3540–3544 (2021).
32. Onoda, S., Sugimoto, N. & Nagaosa, N. Quantum transport theory of anomalous electric, thermoelectric, and thermal Hall effects in ferromagnets. *Phys. Rev. B* **77**, 165103 (2008).
33. Yu, Z.-G. Spin Hall effect in disordered organic solids. *Phys. Rev. Lett.* **115**, 026601 (2015).
34. Davidson, A., Amin, V. P., Aljuaid, W. S., Haney, P. M. & Fan, X. Perspectives of electrically generated spin currents in ferromagnetic materials. *Phys. Lett. A* **384**, 126228 (2020).
35. Taniguchi, T., Grollier, J. & Stiles, M. D. Spin-transfer torques generated by the anomalous Hall effect and anisotropic magnetoresistance. *Phys. Rev. Appl.* **3**, 044001 (2015).
36. Omori, Y. et al. Relation between spin Hall effect and anomalous Hall effect in 3*d* ferromagnetic metals. *Phys. Rev. B* **99**, 014403 (2019).
37. Qu, G., Nakamura, K. & Hayashi, M. First principles investigation of anomalous Hall and spin Hall effects in ferromagnetic CoPt. *J. Phys. Soc. Jpn.* **90**, 024707 (2021).
38. Amin, V. P., Li, J., Stiles, M. D. & Haney, P. M. Intrinsic spin currents in ferromagnets. *Phys. Rev. B* **99**, 220405 (2019).

39. Zhu, L. et al. Strong damping-like spin-orbit torque and tunable Dzyaloshinskii-Moriya interaction generated by low-resistivity $Pd_{1-x}Pt_x$ Alloys. *Adv. Funct. Mater.* **29**, 1805822 (2019).
40. Zhu, L., Ralph, D. C. & Buhrman, R. A. Highly efficient spin-current generation by the spin Hall effect in $Au_{1-x}Pt_x$. *Phys. Rev. Appl.* **10**, 031001 (2018).
41. Ryu, J., Lee, S., Lee, K.-J. & Park, B.-G. Current-induced spin–orbit torques for spintronic applications. *Adv. Mater.* **32**, 1907148 (2020).
42. Zhu, L., Ralph, D. C. & Buhrman, R. A. Maximizing spin-orbit torque generated by the spin Hall effect of Pt. *Appl. Phys. Rev.* **8**, 031308 (2021).
43. Kumar, A. et al. Large damping-like spin–orbit torque and improved device performance utilizing mixed-phase Ta. *ACS Appl. Electron. Mater.* **3**, 3139–3146 (2021).
44. Kumar, A., Bansal, R., Chaudhary, S. & Muduli, P. K. Large spin current generation by the spin Hall effect in mixed crystalline phase Ta thin films. *Phys. Rev. B* **98**, 104403 (2018).
45. Xie, H., Talapatra, A., Chen, X., Luo, Z. & Wu, Y. Large damping-like spin-orbit torque and perpendicular magnetization switching in sputtered WTe_x films. *Appl. Phys. Lett.* **118**, 042401 (2021).
46. An, H., Kageyama, Y., Kanno, Y., Enishi, N. & Ando, K. Spin-torque generator engineered by natural oxidation of Cu. *Nat. Commun.* **7**, 13069 (2016).
47. An, H. et al. Current-induced magnetization switching using an electrically insulating spin-torque generator. *Sci. Adv.* **4**, eaar2250 (2018).
48. Wang, Q., Lu, X., Xin, Q. & Sun, G. Polyol-synthesized $Pt_{2.6}Sn_1Ru_{0.4}/C$ as a high-performance anode catalyst for direct ethanol fuel cells. *Chin. J. Catal.* **35**, 1394–1401 (2014).
49. Rojas-Sánchez, J.-C. et al. Spin pumping and inverse spin Hall effect in platinum: the essential role of spin-memory loss at metallic interfaces. *Phys. Rev. Lett.* **112**, 106602 (2014).
50. Soya, N. et al. Crossover of the intrinsic spin Hall effect in the presence of lattice expansion. *Phys. Rev. B* **103**, 174427 (2021).
51. Obstbaum, M. et al. Tuning spin Hall angles by alloying. *Phys. Rev. Lett.* **117**, 167204 (2016).

Acknowledgements

This work was supported by JST FOREST Program (Grant Number JPMJFR2032), JSPS KAKENHI (Grant Number 19H00864), Canon Foundation, Asahi Glass Foundation, and Spintronics Research Network of Japan (Spin-RNJ).

Author contributions

H.M. fabricated devices. H.M., A.M., and S.H. collected and analyzed the data. K.A. designed the experiments. K.A. and H.M. developed the explanation and wrote the manuscript. All authors discussed results and reviewed the manuscript.

Competing interests

The authors declare no competing interests.

Additional information

Supplementary information The online version contains supplementary material available at https://doi.org/10.1038/s42005-021-00791-1.

Correspondence and requests for materials should be addressed to Kazuya Ando.

Peer review information *Communications Physics* thanks Pranaba muduli and the other, anonymous, reviewer(s) for their contribution to the peer review of this work.

Reprints and permission information is available at http://www.nature.com/reprints

Publisher's note Springer Nature remains neutral with regard to jurisdictional claims in published maps and institutional affiliations.